NEW OPENINGS IN UNREINFORCED MASONRY WALLS UNDER IN-PLANE LOADS: A NUMERICAL AND EXPERIMENTAL STUDY

Abstract: Nowadays existing masonry buildings are frequently modified to satisfy living demands. These modifications may require the addition of new windows or doors in walls of structural functionality. In engineering practice, such modifications are generally designed and verified for vertical loads while, for seismic loads, the changes in the walls' structural behaviour are not yet fully understood. Consequently, current design may incorrectly estimate the in-plane response of the perforated walls. This paper presents an evaluation of the effects of the introduction of new openings in masonry walls under in-plane loads, by a numerical and experimental approach. Two parameters are considered for the numerical studies: opening size and eccentricity. The results show that the loss in stiffness and strength due to new openings are proportional to the opening area and that the eccentricity might change the wall response going from rocking to shear dominant behaviour, depending on the load direction.

Keywords: Openings, eccentricity, unreinforced masonry, in-plane response, numerical modelling.

Biographical notes:

1 INTRODUCTION

Fired clay brick is one of the most common materials used in Unreinforced Masonry (URM) buildings. These buildings are present in countries that have moderate to high earthquake hazard. The vast majority of the URM building stock of these countries was built before the introduction of seismic design recommendations and, nowadays, these buildings are continuously modified to satisfy new functionalities.

Street-level floors, for example, are now used as shops, restaurants or private garages. For their modification, new wide openings for windows or doors towards the street have been cut from originally solid walls (Figure 1). In addition, spaces on the upper floors are often transformed into modern residential

apartments or working spaces. These transformations require new openings to connect adjacent compartments or to add new windows for more natural light.

The problem emerges when these openings are made in structural walls. In fact, introducing new openings in URM shear walls and giving little attention to their position might lead to irregularities and create asymmetrical redistribution of forces when seismic events occur (Figure 2). Some international codes, such as the Italian Design Code (NTC 2018), refer to these types of interventions and suggest that they should be, if possible, avoided in existing unreinforced masonry buildings. When necessary, designers should guarantee that the initial stiffness and in-plane load carrying capacity of the wall with new openings must be equal to the original solid wall (§8.4.1 and §8.4.3 of NTC 2018), in order to prevent modifying the global seismic response.

Thus, in order to design a suitable strengthening technique for such delicate interventions, designers should consider the changes in the structural behaviour of URM walls when new openings are made. In engineering practice, current calculations are based on the "equivalent frame" idealization, where the spandrel contribution is related to the pier's top boundary conditions. Two hypotheses are then available (Lagomarsino et al., 2013): i) the fixed-rotation boundary conditions at the pier ends, that correspond to the "strong spandrel – weak pier" idealization (assumed when very stiff lintels and Reinforced Concrete bond beams are present), and ii) the cantilever idealization, where a "weak spandrel-strong pier" is assumed, i.e., spandrels are poorly connected to the piers and the hypothesis of null strength and null stiffness of the spandrel is adopted. However, evaluations about the performance of unreinforced masonry buildings carried out after the Emilia (2012) and L'Aquila (2016) earthquakes in Italy confirmed the important role of masonry spandrels. Consequently, several authors investigated how the contribution of the masonry spandrel affected the wall's in plane behaviour (Cattari et al., 2008; Milani et al., 2009; Graziotti et al., 2012; Beyer et al., 2012a, 2012b; Parisi et al., 2013, 2014; Rinaldin et al., 2014). They agreed that the spandrel's contribution could be more relevant than the aforementioned two hypotheses, depending on its boundary conditions (based on brick arrangement, lintel type, the presence of ties or reinforced concrete bonding beams) and vertical load acting on the spandrel (which becomes

relevant in the case of irregular arrangements, and which is often the case in buildings with new openings).

New openings create a new spandrel-pier arrangement which may not always be located in line with old openings but in an unconventional position which creates a vertical irregularity in the building's distribution of openings (Figure 1b) and loaded spandrels. Moreover, walls with new openings often include very stiff coupling lintels to satisfy vertical load requirements (e.g. made of steel or reinforced concrete) which are not supported by the quantitative evaluation of their effectiveness under horizontal loads. Walls with new openings with very stiff coupling elements and loaded spandrels can present a different nonlinear behaviour than walls with regular openings and weak elements, which are often present in existing masonry buildings (Cattari et al., 2008, Lagomarsino et al., 2013). More research is therefore necessary, especially in the case of new openings, where a new spandrel might change the previous boundary conditions of the wall panel. In addition the sole action of cutting-out masonry material can debilitate the surrounding masonry and, thus, diminish the pier performance under in-plane loads. Moreover, although it is certain that new openings reduce the in-plane stiffness and strength of the original solid wall, it is useful to provide information on the relationship between the opening size and stiffness/strength loss when seismic forces are applied. This can be done by considering the contribution of the spandrel (which can be subjected to high vertical loads if the opening is located in an irregular position) and not only the performance of the idealized piers, as currently assumed in engineering practice (see Pugi, 2010).

This paper shows the results of a numerical study that was done to simulate perforated masonry walls subjected to monotonic in-plane loading. The numerical analyses herein presented have the aim of providing valuable information for the design of an URM brick wall specimen, built as a solid wall and then perforated and tested under cyclic in-plane loading. For the numerical study, different opening sizes and positions were considered with the aim of evaluating the changes in stiffness and strength of the walls with respect to the solid wall. The research presents spandrels fully loaded in the vertical direction, making the experimental wall specimen somehow different from the H-shape wall specimens tested in Beyer et al., 2012a; 2012b; Graziotti et al., 2012; Parisi et al., 2014; Rinaldin et al., 2014. The paper

aims to contribute to what is already known about the role of a fully loaded spandrel in the overall wall specimen response and failure mode, considering real boundary conditions at the pier-spandrel joints. The experimental results were finally compared to the preliminary numerical results. Furthermore, it was possible to obtain a relationship between the opening area and the loss of stiffness and strength. Finally, the paper includes a short description of the cutting-out process in the chosen masonry wall specimen while a constant vertical load is applied, in order to reproduce the common practice of creating a new door.

2 NUMERICAL MODELS

To assess the effects of a new opening in a real solid wall, the present work uses the macro-modelling technique and the Total Strain Fixed Crack Model (TSFCM), available in the commercial Finite Element Program DIANA v10.1. For masonry models, a micro-modelling, a continuum orthotropic model or a mathematically homogenized technique is often used (Lourenço et al., 1998; Milani et al., 2006). However, these models require a substantial amount of data from specific experimental tests not yet available for the present stage of research activities. By using a non-reliable calibration of the parameters of these models, their predictive performance would be a trial and error process and would not be adequate for the main objectives of this research program at the present stage.

Furthermore, the TSFCM has demonstrated to be capable of properly reproducing the experimental bearing capacity, load deformation response and failure mode of a solid wall, used as reference (SW-R), previously tested at the University of Brescia (Facconi et al, 2015). The suitable prediction of TSFCM is herein demonstrated by comparing the overall response obtained from this approach to that experimentally measured and that determined from the numerical Disturbed Stress Field Model (DSFM). Furthermore, other research works (Giardina et al., 2013; Medeiros et al., 2013; Allen et al., 2017; Ponte et al., 2018) have explored the potentialities of the fixed crack concept and have obtained fair approximations when compared to the experimental results.

2.1 Wall geometry

The wall length *(L_w)*, height *(h_w)* and thickness *(t)* are the following: L_w=3140 mm, h_w=2000 mm and t=250 mm. The wall is representative of a typical URM wall of an Italian building constructed between 1900 – 1950 and reduced by a scale factor of 0.70 (in line with the maximum dimensions allowed by the available test setup).

Models to study the influence of the opening area

In this work, the opening area (*OA*) is defined as the ratio of the perforated area to the total wall area expressed in percentages. In this context, three models of increasing width and height were considered (Figure 3a):

1) Model ***PW+L(sw): P****erforated* ***W****all* with ***L****intel* and a ***S****mall* ***W****indow* (OA= 8.5%);
2) Model ***PW+L(lw): P****erforated* ***W****all* with ***L****intel* and a ***L****arge* ***W****indow (OA*= 21%);
3) Model ***PW+L(dc): P****erforated* ***W****all* with ***L****intel* and a ***D****oor* ***C****entred* (OA=19%).

Models to study the influence of the opening position

The eccentricity (x_e) of the wall is defined as the distance between the door and the centre of the wall of geometry (x_0) divided by half the length of the wall (expressed in percentage). Herein, three possible locations for the door opening are modelled (Figure 3b):

1) Model ***PW+L(dc)***: wall with a centred door. For this model eccentricity e=0% since the door and wall centre are aligned.
2) Model ***PW+L(d25e)***: wall with an eccentric door of x_e*=25%*.
3) Model ***PW+L(d50e)***: wall with an eccentric door of x_e=50%.

The geometry of these models is summarized in Figure 3 and Table 1.

2.2 Mesh, constraints and loading conditions

Quadrilateral isoparametric 8-node plane stress finite elements of about 70 mm in size and 2x2 integration points (i.p.) according to the Gauss-Legendre integration technique are used (Figure 4). Mesh sensitivity analyses were carried out in a previous research (Ona, 2018), where the results showed mesh independency for a crack bandwidth *(h)* defined as the square root of the total area of the element (Diana TNO User's Manual, 2016).

The walls were modelled as cantilever beams with the nodes at the base line horizontally and vertically restrained (Figure 4). The masonry properties are shown in Table 2. At the top of the opening a lintel was modelled as a linear elastic material with a Young Modulus (E_c) of 27000 MPa and Poisson coefficient (ν_c) of 0.20. The lintel elements were the same plane stress elements used for masonry material and were in perfect contact with the masonry wall (interfaces were not used). The concrete beam (with E_c=30000 MPa and ν_c =0.20), used in the laboratory to uniformly distribute the load along the wall specimen, was also modelled as a linear elastic material perfectly connected to the masonry wall.

Loads were applied in two phases:

- Phase 1) application of a distributed pressure of 0.32 MPa (250 kN of vertical load);
- Phase 2) application of a monotonic increasing horizontal displacement.

The vertical load of Phase 1) is representative of a two-storey house; a monotonic loading was chosen instead of the cyclic loading because the simulations aimed to capture the walls lateral capacity, initial stiffness and possible failure mechanisms. The evaluation of the energy dissipation or sharp reproduction of the experimental load-displacement hysteresis curves were not within the frame of this work.

2.3 Material properties and constitutive relations

The inelastic deformation of masonry in compression was simulated by a parabolic stress-strain relationship that includes a softening stage (Figure 5a), while the fracture mode I propagation was

158 modelled by the exponential curve proposed by Hordjik, 1991 (Figure 5b). Crack bandwidth *h* used to
159 assure mesh objectivity was defined as the square root of the total area of the element, as suggested in
160 Diana TNO User's Manual, 2016. The post-cracked shear stiffness, ($G_{cr}= \beta G$), was simulated by an
161 almost-zero value of the shear reduction factor ($\beta= 0.01$ to avoid numerical inconsistences). This β value
162 is suitable for model brittle ceramic materials such as masonry, where the aggregate interlocking effect
163 is significantly reduced and, consequently, almost-zero shear stresses are transferred upon cracking
164 (Rots and Blaauwendraad, 1989).

165 The remaining values that characterize the material properties were taken from the available exper-
166 imental data and recommendations from the literature. To verify the applicability of these properties
167 when using the TSFCM, the numerical results of the TSFCM were validated against the experimental
168 envelope of the SW-R cyclic in-plane test and against the numerical curve obtained by Facconi, 2013
169 using the Disturbed Stress Field Model for Unreinforced Masonry (DSFM-URM).

170 The major difference between the TSFCM and the DSFM in the context of modelling URM is
171 mainly restricted to the simulation of the compression behaviour. The compressive constitutive law for
172 the TSFCM considers the material as an isotropic continuum; therefore, the elastic behaviour depends
173 on one value of the Young Modulus and Poisson coefficient. The DSFM-URM on the other hand con-
174 siders the orthotropy of masonry from its elastic branch and the Young Moduli in two directions (-x and
175 -y). The DSFM-URM is an advancement of the DSFM initially developed for reinforced concrete (Vec-
176 chio, 2000) and it is based on the Ganz failure criterion. Further details about this model and its formu-
177 lation may be found in Facconi, 2013.The values of the parameters used in this paper are indicated in
178 Table 2.

179 **2.4 Model validation**

180 The envelope of the experimental cyclic curves and the numerical response of SW-R are compared
181 in Figure 6, where very good agreement is verified. In particular, the ultimate displacement predicted

by the TSFCM (at 6.49 mm, which corresponds to the last converged step) is closer to the experimental value (of 4.98 mm) than the DSFM-URM model (10.35 mm).

Figure 7 shows the numerical and the experimental crack patterns at different values of the horizontal displacement. In the TSFCM, crack width is estimated as the product of the crack tensile strain and crack bandwidth *h*. A good agreement can be observed between experimental and numerical crack patterns. At a displacement of 0.7 mm a sliding crack started to develop (Crack A) while at a displacement of 2.95 mm (drift=0.15%) the right toe of the wall started to crush. Finally, a diagonal crack (Crack C) formed along the wall. These cracks evolved until the end of the test. As observed experimentally, diagonal and sliding cracking were the main failure mechanisms predicted by the numerical model.

3 NUMERICAL RESULTS

In this section, the influence of the opening size and the opening position of the models described in Figure 3 are presented. The material parameters, FE mesh and boundary conditions were the same as SW-R. The analyses were stopped when no further convergences were found for small tolerances based on energy and displacement convergences (0.001 and 0.01 respectively), in line with model SW-R. The vertical load was imposed in force control while the lateral load was applied in displacement control with a maximum and minimum load step-size of 0.05 and 0.01, respectively. The analyses were solved by using the modified Newton Raphson method.

3.1 Influence of the opening size

From Figure 8, the decrease in percentage of Shear Strength (*V*) and stiffness (*K*), when creating an opening with a vertical axis coincident with the geometric centroid of the wall (i.e., eccentricity=0), seems to be framed in the following intervals:

$$1.5\,OA \leqslant \Delta V \leqslant 2.0\,OA \quad (1)$$

$$2.1\,OA \leqslant \Delta K \leqslant 2.5\,OA \quad (2)$$

where, *OA* is the opening area expressed in a percentage (Table 1), *ΔK* and *ΔV* are the variation of in-plane stiffness and shear strength, respectively, and expressed in a percentage. The initial stiffness *K* is evaluated at a wall displacement of 0.25 mm in the load-displacement curve shown in Figure 8. The results of model PW+L(dc) will be compared against the first cycles of the experimental load-displacement curve shown in Section 5.

Figure 8, shows that the stiffness decreased with increasing length of the opening span. Larger opening spans entail slender piers. Since the pier stiffness is dependent on the pier cross section, the shear load-lateral displacement curves are in line with this concept.

Figure 9 presents the principal stresses and strains at the last step of the analyses showing a mixed behaviour for walls SW-R, PW+L(sw) and PW+L(dc): the compressive strut started from the loading point and flowed through the spandrel and lintel to the opening's right corner and finished at the right toe of the right pier. The concentration of compressive stresses at the wall toe and the compressive strut generated tensile stresses along the pier diagonal, which induced cracks along the strut in later steps. The vertical tensile stresses were generated on the left side of the wall when the wall was being pushed and therefore created the typical flexural bed-joint cracks. In wall PW+L(lw), the tensile stresses were concentrated orthogonal to the diagonal strut on the right pier, indicating dominant shear behaviour.

3.2 Influence of the opening position

The results of the previous section indicate that the loss in stiffness due to new openings is proportional to the opening width. In the present models with a door having an opening area *OA*=19% (Figure 4, right column), the decrease of lateral wall stiffness was ~~approximately~~ equal to ~~varies between~~ -41% ~~and -45% for a centred door PW+L(dc) and for an eccentric door PW+L(d50e) in the negative~~in both loading direction~~s, respectively~~. The results are in line with Equation 2 (Section 3.1)~~2~~. Furthermore,

~~I~~in these models, the loss of initial stiffness (calculated at lateral displacement δ=~~±~~0.25 mm) seems to be independent of the location of the opening. Although this might be true for the two eccentricity ratios and for the typology of the wall studied herein, the present results are ~~in line~~consistent with the

results obtained by Billi et al., (2018), who found a stiffness reduction of about 50% for non-centroidal openings (of similar OA%) with eccentricity percentages between 30%-50%. The in-plane strength reduction also seems to be influenced by the load direction. Therefore, the results are evaluated in both, positive (+x) and negative (-x) loading directions. Figure 10 shows the load-displacement curves of the models and indicates that the response is governed by mixed behaviour. The principal stresses and strains (Figure 11-12) confirm this behaviour and indicate that collapse is governed by the simultaneous occurrence of excessive compressive deformation in the strut and by the formation of macro diagonal cracks in the same critical zone.

The particular response of wall PW+L(d25e) in the negative direction should be observed. It shows a brittle response at a displacement δ=-4.5 mm due to a dominant shear behaviour evident in Figure 11 where the tensile strains along the diagonal of the left pier are shown. The shear dominant behaviour is typically characterized by smaller values of ultimate displacement than a rocking dominant behaviour. Therefore, the numerical curve of PW+L(d25e) in the (-x) load direction is in line with the failure mechanism of the wall.

From the principal stresses and strains presented in Figures 11 and 12, one can observe, that the stress flows from the load point of application, through the spandrel to the opposite bottom corner. In a solid wall, the stress flows along the diagonals of the rectangular or square shape of the wall (Figure 9a). Conversely, in walls with openings, the opening represents a discontinuity for the stress flow and thus concentrates the compressive strut along the pier opposite to the load point of application.

The principal strains from Figure 11 also indicate that the cracks of model PW+L(d25e) are fairly symmetrical in the (+x) and (-x) load direction, suggesting dominant shear behaviour. For model PW+L(d50e), the principal strains in the (+x) direction indicate mixed flexural-diagonal crack behaviour, while in the (-x) direction they indicate dominant flexural behaviour.

The aforementioned results are in line with the analytical models available in the literature. The shear capacity of a masonry wall when diagonal cracking occurs is determined by Equation (3) according to the formulation of Turnšek and Cacovic, 1970:

$$V_{max,d} = \frac{f_t \cdot L_p \cdot t}{b}\sqrt{\left(1 + \frac{\sigma_m}{f_t}\right)} \quad (3)$$

where: σ_m=mean vertical pressure acting on the wall, L_p=pier length, t=wall thickness, f_t= tensile strength, ~~β~~ b=1.5 for walls with a height-to-length ratio of $h/L_p \geqslant 1.5$, $b = h/L_p$ for $1.0 < h/L_p < 1.5$ and ~~β~~ b =1.0 for $h/L_p \leqslant 1.0$. Since walls are assumed as cantilever beams and for simplicity, $h=h_w$ herein.

When assuming constant material properties, wall thickness and vertical load in Equation (3), the diagonal shear strength becomes dependent on the masonry pier length *(L_p)*. This means that the wider the pier, the higher the wall shear capacity, which is in line with the trend of the V-δ curves shown in Figure 10. ~~As far as the stiffness strength is concerned, Figure 10 shows that~~Furthermore, it should be noted that the loss of ~~stiffness~~ strength of walls PW+L(d25e) and PW+L(d50e) in the negative load direction is greater (-~~45~~37% and -46%, respectively) if compared with the positive one (-10~~41~~% and -18%). This difference can probably be attributed to the position of the door opening: when the eccentricity of the door is opposite to the load direction, the system can benefit from the activation of a compressive strut in the larger pier. On the contrary, when pushing toward the negative direction, the resisting mechanism mainly relies on the flexural behaviour of the two piers, as shown by the pattern of the principal stress and strain in Figure 11 and Figure 12.

4 IN-PLANE TEST OF A WALL WITH CENTRAL DOOR OPENING

Because door openings are one of the most typical local intervention in two-storey dwellings, this configuration was selected for the following experimental test. The centred position was preferred to reduce further uncertainties in the experimental program. The brick type and bonding pattern are similar to the solid wall of reference SW-R (Facconi et al., 2015). However, differences in the mechanical properties of the masonry used herein and the one used by Facconi et al. (2015) are possible. The outcomes of this test will be later compared against the numerical results.

Field Code Changed

Formatted: Not Highlight

4.1 Materials, geometry and vertical load

The solid brick geometry (240 mm x 110 mm x 50 mm), the mortar, the wall overall dimensions, the average vertical pressure and testing conditions were similar to the ones used in Facconi et al. (2015), in order to be able to compare the results between solid wall SW-R and perforated wall PW+L(dc). The opening geometry and position were equal to model PW+L(dc) of Section 2.1. The cutting-out process and the following in-plane test were both carried out under a constant vertical load of 250 kN, representative of the force acting on the ground wall of a two-storey masonry building. This load corresponds to a distributed pressure of 0.32 MPa (σ_v), which is equal to 5.3% of the masonry compressive strength. The load was applied by a vertical hydraulic jack (Figure 13a) and was distributed through steel beams placed on the top of a concrete beam. The vertical jack was self-balanced with a beam rigidly anchored to the laboratory strong floor by means of two hinged vertical steel bars.

4.2 Cutting-out process for the new opening

The vertical pressure applied by the hydraulic jack was manually maintained constant during the cutting-out process in order to better simulate the real practice when creating a new opening. Prior to the perforation process, a diamond grinding disk was used to cut two straight vertical lines of 1400 mm inside the wall. After this process and before removing all the bricks from the future opening, a temporary support over the forthcoming door was installed to avoid a possible collapse (Figure 13a).In fact, four props were placed on each side of the wall to shore up a beam installed in the wall thickness (Figure 13b). Later, the bricks were removed, one by one, by means of a hammer drill and a masonry bit that was used to drill holes in the mortar between the bricks. After drilling, the mortar became softer and the bricks could be easily removed from the wall; therefore, no excessive workforce was needed and possible damage due to excessive vibrations was prevented.

The structural lintel, composed of two steel profiles HEA120, was designed according to recommendations from the Technical Notes on Brick Construction, BIA-31B, 2011 and DIN-1553, 1952. The two

steel profiles were connected by two M12 threaded rods, one on each side of the lintel, which was fixed to the wall with a surrounding mortar having a compressive strength of f_c=20 MPa (Ona, 2018). The bedding area was 170 mm x 250 mm. Once the mortar had dried, the masonry in the bottom of the lintel and the supporting props were removed. This perforation process guaranteed a partial re-distribution of vertical stresses, forming the natural arching action in masonry walls with openings (Figure 14a). After the cutting-out process, some small cracks at the spandrel level were observed (Figure 15b); moreover, a crack along the wall mortar bed-joint, at the base of the right pier, was noticed after the intervention (Figure 15c). This crack was probably caused both by small natural eccentricities of the vertical load and by the settlement of the new pier when fixing the wall base to the laboratory strong floor with tensile bars (Figure 14b).

4.3 Test set up

The wall was tested by applying variable horizontal cyclic displacements through a concrete top beam at the top of the wall and an electromechanical jack having a 500 kN capacity, fixed to a reacting steel braced frame already used in former experimental research (Facconi et al., 2015; Messali et al., 2017). As shown in Figure 16, the jack was connected to the steel loading plate 1 which pushed the loading cell and the Reinforced Concrete (RC) distributor top beam towards the right (positive loading direction). A steel bar running through the mid-section of the RC beam was connected to steel plate 2, which pulled the wall towards the left (herein assumed negative loading direction). The lateral displacement history used is shown in Figure 17; three full cycles were applied up to a lateral displacement of about 6.0 mm, corresponding to a drift of about 0.4%. Afterwards, the axial load was increased to 400 kN (σ_v =0.51 MPa) before continuing the cyclic loading. This second part of the test is found elsewhere (Ona, 2018).

The wall was instrumented with Linear Variable Differential Transformers (LVDT) and potentiometers used to register the wall deformations and the crack opening. The four (more relevant) instruments used are shown in Figure 16: LVDT H_1 recorded the lateral displacements of the wall with reference to

the laboratory strong floor; LVDT H_2 recorded possible slippage between the concrete foundation and the laboratory strong floor; LVDT V_1 and LVDT V_2 recorded any rotations of the concrete basement. Further instruments were used to measure the bed-joint crack opening (~~LVDT~~V3, V4, V5, V6), possible flexural or shear mechanisms on and spandrel (D1 - D6) and piers (D7 - D10). Further details can be found in (Ona, 2018).

The lateral displacement of wall (δ) and drift (d_r) are determined as:

$$\delta = \left(\delta_{x,H1} - \delta_{x,H2}\right) - \left(\frac{\delta_{y,V1} - \delta_{y,V2}}{L_{V1-V2}}\right) \textit{H}_{H1-H2} h' \quad (4)$$

$$d_r[\%] = \frac{\delta}{h'} \cdot 100 \quad (5)$$

where $\delta_{x,H1}$, $\delta_{x,H2}$, $\delta_{y,V1}$, and δ_{yV2} are the displacements measured by the *LVDTs* H_1, H_2, V_1 and V_2 respectively; $L_{V1\text{-}V2}$ and $h' = H_{H1\text{-}H2}$ are the horizontal and vertical distance between the measurement devices (~~H1-H2 and~~ V1-V2 and H1-H2), as shown in Figure 16.

5 EXPERIMENTAL RESULTS

5.1 Load carrying capacity

The wall response was dominated by flexural behaviour, initiated by horizontal (bed-joint) cracks along the base of both piers and followed by severe damage at the spandrel level. At the end of the test (δ=6 mm, d_r=0.40 %), a diagonal (stair-stepped) crack formed at the pier-spandrel while the flexural bed-joint cracks were noticeable along the pier (whole) cross section. The overall lateral force-displacement curve is plotted in Figure 18, which shows a small difference in the initial elastic stiffness (K_e): for positive displacements K_e^+=+101 kN/mm while for negative displacements K_e^-=-125 kN/mm (both measured at δ=+/-0.25 mm). Although the opening was positioned symmetrically, the bed-joint cracks observed after the perforation process (see Section 4 and Fig. 15b) and prior to the in-plane test contributed to this asymmetric response. When loading the wall towards the positive direction, pre-test cracks ~~were located~~ at the base of~~in~~ the compressive strut of pier 2 ~~, thus~~ impaired~~ing~~ the

Field Code Changed

Field Code Changed

Formatted: Indent: First line: 5 mm, Space After: 2 line, Don't add space between paragraphs of the same style

Formatted: Not Highlight

Formatted: Font: Not Italic

Formatted: Font: Not Italic

Formatted: Font: Not Italic

Formatted: Font: Not Italic

stiffness the wall with respect to the negative direction. Figure 18 shows a less resistant response in the positive direction with respect to the negative with a peak shear load of 129 kN and 175 kN, respectively. While in the negative direction the wall exhibited a flexural failure mechanism ~~was governed by the flexural behaviour~~ reaching a peak load close to upper limit of the rocking behaviour (187 kN), in the positive direction the wall behaviour was governed by mixed flexural-shear mode failure with the onset of shear damage in the pier 2, thus limiting the wall capacity, as also discussed in the following section.

5.2 Cracking patterns

The ~~final cracks~~cracking patterns from the experimental test are schematized in Figures 19. The cracks started developing at a lateral displacement (δ) of 1 mm (d_r=0.05%). The first cracks were horizontal and were observed along the base and at the middle height of pier 2. A diagonal crack along pier 1 started from the left corner of the lintel and continued to develop for the next cycles until d_r=0.25% (Fig 19a). The propagation of the crack at the middle height of pier 2 continued until the end of the test (d_r= 0.40%). At this displacement, the crack reached the bottom corner of the steel lintel. Cracks at the base of piers 1 and 2 started at d_r=0.05% and finished at d_r=0.25%. The spandrel developed a mixed flexural-shear failure, with vertical cracks at the end of the lintel and stair-stepped shear cracks in the spandrel. It was observed that the cracks were symmetrical when comparing the front and back views, while a certain amount of asymmetry was evident when comparing cracks from pier 1 to pier 2. This asymmetry seems to be consistent with the behaviour observed in the hysteresis shown in Figure 18, where the wall seems to be stiffer in the negative load direction and more flexible in the positive load direction with also larger residual displacements. The reason for this asymmetry might be related to the natural heterogeneity of masonry and the pre-test bed-joint cracks observed along the pier 2 (Figure 14b and 15b) which tend to close when the load acts in the positive direction, thus impairing the flexural stiffness of the pier 2. On the contrary, in the negative direction, the pre-test cracks are discontinuities

Formatted: Not Highlight

which grow with the application of the in-plane load without affecting the behaviour of opposite pier 1-. In fact, the first crack observed during the test (at δ=1.0 mm, in Figure 19a), developed along the plane of the bed-joint crack of pier 2. Similar cracks are possible during a real intervention in a masonry wall (which is loaded) and can create further planes of weaknesses that are unfavourable for the wall's strength and stiffness, which are both already reduced due to the new opening cut.

Finally, the instruments placed on the diagonals of both piers allowed to measure their angular deformation, evaluated as the sum of the strains along the diagonals. As shown in Figure 19d the measured shear deformation of pier 2 for positive drift was as twice as great the angular deformation of pier 1 for the negative direction. This experimental evidence proves the possible onset of micro-shear damage in the pier 2 along with flexural cracks at the base of the piers and diagonal/flexural cracks in the spandrel. It should be also observed that the measured shear damage which was not clearly eye-visible when the test terminated.

Based on the formulations proposed by Giordano et al., 2006 it is possible to identify two collapse mechanisms for this wall (these formulations are mainly based on the masonry wall geometry). The obtained results are in agreement with the experimental cracks observed after the test, as shown in Figures 19b,c, where the two possible mechanisms are highlighted. It is then concluded that the wall response involved mainly rocking of both piers with flexural and shear cracks in the spandrel, sliding at mid-height of Pier 2 and moderate shear-damage in the pier 2.

Formatted: Not Highlight

5.3 Solid Wall vs Wall with an opening

In Figure 20, the experimental positive and negative envelope curves from cyclic loading on PW+L(dc) are compared against the experimental curves obtained from the reference Solid Wall (SW-R) tested in Facconi et al. (2015). Since SW-R had similar dimensions to PW+L(dc) (3070 mm x 2170 mm x 250 mm) and was tested under the same set-up and loading conditions, a comparison between the lateral load-displacement curves and crack patterns is possible.

From Figure ~~21~~20, it is observed that PW+L(dc) is much more deformable than SW-R. This is summarized in Table 3 where the elastic stiffness is measured at a wall displacement (δ) equal to 0.25 mm (in positive and negative directions). PW+L(dc) presents an average (from the +x and -x direction) reduction of the initial stiffness (with respect to the SW-R) of about 45%. Similarly, the average peak load decrease is about 22%; these values are in line with the numerical prediction described in Section 4.1 and Equation (1) and (2).

It is worth noting the difference in the wall's response when the horizontal jack was pushing or pulling the wall. This variation can be mainly attributed to the bed-joint crack on pier 2, formed after the perforation process, thus prior to the in-plane test. When pushing the wall, the shear strength increased only when the bed-joint crack width was completely closed; this caused a change in the slope of the cycles in the positive load direction that was not observed for the negative cycles. Since bed-joint cracks were not observed in the left pier, it is reasonable to think that the wall response in the negative-load direction is stiffer and the peak load attained may be higher than in the positive direction.

Finally, from the cracks observed in solid wall SW-R (Figure 6) and in the wall with an opening (Figure 19), one can note that the failure mechanism changed from mixed flexural/diagonal cracking to flexural combined with shear damage in the spandrel and the right pier for positive direction and flexural behaviour for the negative one.~~a rocking behaviour with a lower lateral resistance.~~

Formatted: Not Highlight

5.4 Experimental vs Numerical results

The numerical and experimental load-displacement curves of PW+L(dc) and SW show that the loss in stiffness (~~about~~ equal to ~~40~~1% and 45%, respectively) due to the new centred opening is proportional to the opening ~~width~~ area (OA=19%), as already discussed in Section 3.1. ~~In the present models (Figure 4, right column), the opening area is constant (OA=19% in all cases), and the drop in stiffness is 41%, which is in line with Equation 2 (Section 3.1).~~ Since the cyclic envelope curve was not symmetric in the positive and negative loading directions (due to the bed-joint crack on pier 2), the numerical simulation

was not capable of capturing the influence of the pre-damage caused by the cutting process on the wall's response (Figure 20).

In the numerical simulations, these pre-existing cracks were not considered, since this would require the implementation of interface finite elements, with detrimental consequences in the complexity of the mesh and computing time. Furthermore, and this is even more important, it would be too difficult to have a reliable procedure to define the constitutive laws of these interface finite elements. Therefore, the authors decided not to include the pre-damage in the numerical simulations, even though they are aware of the fact that these assumptions may have consequences on the accuracy level of the simulations. One of these consequences is the crack pattern, since the pre-existing crack at the bottom of Pier 2 transformed into a macro-crack. Instead, numerical simulations promoted the prediction of a diagonal shear failure crack because the pre-existing macro-crack was not modelled. The critical analysis of the performance of the numerical simulations should focus on the stiffness degradation, as well as on the load carrying capacity during the imposed displacement process, and in this regard, the simulations can be considered quite satisfactory.

The initial stiffness (at δ=0.25 mm) and ultimate displacement were predicted with fair accuracy by the numerical model. For a better approximation of the stiffness degradation (from δ=0.25 mm to δ=2.3 mm) and the in-plane strength, numerical simulations could include an interface to simulate important cracks observed during/after the cutting out process or could reduce the Young Modulus in the case of several small cracks distributed along piers or spandrel. Figure 21 shows the numerical and experimental crack pattern for wall specimen PW+L(dc); it can be observed that the model is able to capture flexural cracks (bed-joint cracks along wall piers), spandrel damage and cracking at the lintel corners. ~~F~~Furthermore, the numerical model shows an evident ~~-~~diagonal crack along pier 2 which was not clearly visible~~-~~ during the experimental test. However, the higher shear deformation of pier 2 with respect to pier 1 measured during the test (Fig. 19d) may prove the onset of shear damage in pier 2 as it is shown by numerical analysis.

Two hypotheses are proposed for the inaccuracy of numerical model PW+L(dc) in the prediction of the diagonal crack:

Hypothesis 1) since the experimental test was stopped before collapse (at δ=6.7 mm), with the aim of carrying out a second test under a 400 kN vertical load, this diagonal crack did not occur as a secondary damage event during this test. The feedback for this hypothesis is in line with the statement of Magenes and Calvi, 1997: *"in case of a pure flexural response, i.e., of a potential rocking response, very large displacements can theoretically be obtained without significant loss in strength, especially when the axial load is low compared to the compressive strength of masonry. These large displacements can be limited by a second collapse event"*. In this case, the secondary event could have been the diagonal crack if the test had been subjected to larger displacements. This hypothesis is proposed only for this wall as its difference between rocking and shear limit resistance is very small when calculated as follows: the rocking resistance is calculated from simple equilibrium: $V_r = \frac{P_v L}{2 H_0}$ = 187 kN where P_v=250 kN is the vertical load applied, L =3150 mm and H_0=2100 mm are the length and height of the wall respectively (see Figure 16), while the shear capacity is calculated from Eq. (3) and is equal to 198 kN (assuming the contribution of the lintel in coupling the piers and the effective height and length equal to the wall's total height and length).

Hypothesis 2) the lintel embedded length in the masonry wall (about 170 mm depth) improves the in-plane wall stiffness by strengthening the spandrel. However, it also divides the piers at their mid-height. After the local intervention, a bed-joint crack at the mid-height of the right pier (front view) was observed for a second specimen (not shown herein). It cannot be excluded that this crack might have occurred in Specimen PW+L(dc) too, since the construction and perforation conditions were similar for both specimens. In fact, one of the first cracks that developed during the in-plane test was observed at mid-height of this right pier (Crack C, in Figure 19a). This crack along with the crack at the base (Figure 14) represent planes of weakness along which cracks propagate during the test; the latter are not included in the initial numerical model and could have reduced the accuracy of the numerical cracks.

6 CONCLUDING REMARKS

The paper presents numerical and experimental results on the effects of new openings in masonry shear walls subjected to in-plane loading. The following outcomes can be drawn:

- New openings in existing walls may have a significant impact on wall behaviour when submitted to in-plane forces. In case of large openings (such as doors), the wall's resisting area is considerably reduced; therefore, the wall's horizontal stiffness decays and, depending on the position of the opening inside the building, the remaining shear walls might be subjected to larger in-plane forces. Furthermore, the new piers of the walls with openings might experience larger displacements and brittle failure with respect to the original configuration.
- According to the numerical models, based on the Total Strain Fixed Crack Model (TSFCM), the loss in lateral strength is proportional to the opening area. The percentage of loss in strength is approximately 1.5 to 2.0 times the opening area (as a percentage of the initial wall). A similar proportion is observed for the loss in stiffness, which is about 2.1 to 2.5 times the opening area. However, the opening width can have a higher impact on the wall response, with respect to the opening depth.
- Experimental results from a wall with an opening confirmed the expected predictions since the initial stiffness decreased by about 45% and the peak load by about 22% (with respect to a solid wall). However, the peak load of the wall with the opening is greater than that of the solid wall tested in a previous research (Facconi et al., 2015). It should be noted that the two walls present different mechanical properties; in fact, the two walls were built with different batches of bricks and mortar. Furthermore, the contribution of the presented lintel in coupling the piers was also noticeable.
- On site operations to make the new wall may provoke some cracks in the wall due to the stress deviation and redistribution; therefore, on-site operations should be properly planned in order to

limit the formation of new cracks. Similarly, laboratory experiments are more representative of a real situation if the new opening is made in the wall under vertical loads, as done in the present research study.

- Cracks that developed during on-site operations may influence the response of the seismic performance of the wall due pre-existing planes of weaknesses (such as the initial horizontal crack).
- The experimental crack patterns of the walls tested suggest that the original wall experienced mixed flexural and shear diagonal behaviour while the wall with a new door mainly experienced a flexural behaviour of the lateral piers, ~~separated by the new wall~~shear cracks in the spandrel, sliding at mid-height of Pier 2 and moderate shear-damage in the pier 2.

Formatted: Not Highlight

7 ACKNOWLEDGEMENTS

The authors would like to thank Eng. Student 1 and Student 2 for their contribution and support throughout the tests and data processing. A special thanks also goes to the laboratory technicians ….for their support in the experimental activities.

Formatted: Highlight

8 REFERENCES

Allen, C., Masia, M., Page, A., Griffith M., Ingham, J. (2017) 'Nonlinear finite element modelling of unreinforced masonry walls with opening subjected to in-plane shear'. Paper presented at the13th Canadian Masonry Symposium. 4th – 7th June 2017. Halifax, Canada.

Beyer, K., Dazio A. (2012a) 'Quasi-static monotonic and cyclic tests on composite spandrels'. Earthquake Spectra; Vol 28(3), pp. 885–906.

Beyer, K., Dazio A. (2012b) 'Quasi-static cyclic tests on masonry spandrels'. Earthquake Spectra; Vol 28 (3), pp. 907–29.

517 BIA-31B (2011) Brick Industry Association, Technical Notes on Brick Construction, No 31B: 'Struc-
518 tural Steel Lintels. Allowable Stress Design of Concrete Masonry Lintels based on the 2012
519 IBC/2011 MSJC', TEK 17-1D. National Concrete Masonry Association.
520 Billi, L., Laudicina, F., Salvatori, L., Orlando, M., Spinelli, P. (2019) 'Forming new steel-framed
521 openings in load-bearing masonry walls: design methods and nonlinear finite element simulations'
522 *Bulletin of Earthquake Engineering*, vol. 5, no. 17, pp. 2647-2670.
523 DIANA Finite Element Program (2016) 'Diana user's manual. Release 10.1'. The Netherlands.
524 DIN 1053 (1952), 'Mauerwerk - Berechnung und Ausführung', Germany.
525 Facconi, L. (2013) 'Fiber Reinforced Concrete and Mortar for enhanced structural elements and struc-
526 tural repair of masonry walls', PhD Thesis, Università degli Studi di Brescia, Italy.
527 Facconi, L., Conforti A., Minelli, F., Plizzari, G., (2015) 'Improving shear strength of unreinforced
528 masonry walls by nano-reinforced fibrous mortar coating', Materials and Structures 48, pp. 2557-
529 2574. DOI 10.1617/s11527-014-0337-0
530 Parisi, F., Augenti, N. (2013) 'Seismic capacity of irregular unreinforced masonry walls with openings',
531 Earthquake Engineering & Structural Dynamics, vol. 42, no. 1, pp. 101-121.
532 Parisi, F., Augenti, N., Prota A. (2014) 'Implications of the spandrel type on the lateral behavior of
533 unreinforced masonry walls', Earthquake Engineering & Structural Dynamics, vol. 43, pp. 1867-
534 1887.
535 Gattesco, N., Clemente, I., Macorini L, Noè S. (2008) 'Experimental investigation on the behaviour of
536 spandrels in ancient masonry buildings', Paper presented at the 14th WCEE Conference, Beijing,
537 China.
538 Giardina, G., Van de Graaf, A., Hendriks, M.A.N., Rots, J.G., Marini, A. (2013) 'Numerical analysis of
539 a masonry façade subjected to tunneling-induced settlements', Engineering Structures Vol 54, pp.
540 234-247.
541 Giordano, A., De Luca, A., Mele, E., Romano, A. (2006) 'A simple formula for predicting the horizontal
542 capacity of masonry portal frames'. Engineering Structures; Vol 29, pp. 2109–2123.

543 Graziotti, F, Magenes, G, Penna, A. (2012). 'Experimental cyclic behaviour of stone masonry spandrels'.
544 In: Proc. 15th WCEE, Lisbon, Portugal.
545 Hordijk, D.A. (1991) 'Local approach to fatigue of concrete'. PhD Thesis, Delft University of Technol-
546 ogy, Delft University Press, Delft (NL).
547 Cattari, A., Lagomarsino S. (2008) 'A strength criterion for the flexural behaviour of spandrel in un-
548 reinforced masonry walls' in 14th World Conference on Earthquake Engineering, Beijing, China.
549 Lagomarsino S., Penna A., Galasco A., Cattari S. (2013), 'TREMURI program: An equivalent frame
550 model for the nonlinear seismic analysis of masonry buildings'. Engineering Structures, vol. 56, pp.
551 1787-1799.
552 Lourenço P.B., Rots J.G., Blaauwendraad J. (1998) 'Continuum model for masonry: parameter estima-
553 tion and validation'. Journal Structural Engineering, ASCE, Vol 124 (6), pp. 642-52.
554 Magenes G., Calvi G.M. (1997) 'In-plane seismic response of brick masonry walls'. Earthquake Engi-
555 neering Structural Dynamics. Vol. 26: pp. 1901–1112.
556 Medeiros, P., Vasconcelos, G., Lourenço, P.B., Gouveia, J. (2013) 'Numerical modelling of non-con-
557 fined and confined masonry walls'. Construction and Building Materials; Vol 41, pp. 968-976. DOI
558 10.1016/j.conbuildmat.2012.07.013
559 Messali, F., Metelli, G., Plizzari, G. (2017) 'Experimental results on the retrofitting of hollow brick
560 masonry walls with reinforced high performance mortar coatings'. Construction and Building Ma-
561 terials, Vol 141, pp. 619-630. DOI 10.1016/j.conbuildmat.2017.03.112.
562 Milani, G., Lourenço, P.B., Trali, A., (2006) 'Homogenized limit analysis of masonry walls. Part I:
563 failure surfaces'. Journal Computer & Structures; Vol 84 (3-4), pp. 166-80.
564 NTC (2018). 'Decreto Ministeriale Norme tecniche per le costruzioni. Ministry of Infrastructures and
565 Transportations'. G.U. S.O. n.42 on 20/2/2018; 2018 (in Italian).
566 Ona, M. (2018) 'Local interventions in unreinforced masonry walls: new openings and seismic retrofit-
567 ting strategies'. Unpublished PhD Thesis, Università degli Studi di Brescia, Italy.

Ponte, M., Milosevic, J., Bento, R., (2018) 'Parametrical study of rubble stone masonry panels through numerical modelling of the in plane behaviour' Bull Earthquake Eng. Vol 17 (3), pp. 1553-1574 https://doi.org/10.1007/s10518-018-0511-9.

Pugi, F. (2010) 'Interventi nelle murature e nuova normativa sismica: Aperture e cerchiature in murature portanti con telai in acciaio e in calcestruzzo armati, analisi conforme alla normativa NTC 2008', regione di Toscana: D.G.R. 606 del 21/06/2010) [in Italian], Ed AEDES, ISBN 9788860555663.

Rots, J.G. and Blaauwendraad J. (1989) 'Crack models for concrete: discrete or smeared? Fixed, multi-directional or rotating?'. Delft University of Technology, Delft. The Netherlands.

Turnšek, V. and Cacovic, F., (1970) 'Some experimental results on the strength of brick masonry walls'. In Proceedings of the 2nd International Brick Masonry Conference, Stoke-on-Trent, UK, 12–15 April 1970.

Vecchio, F. (2000) 'Disturbed stress field model for reinforced concrete: formulation'. Journal Structural Engineering ASCE, vol. 126, no. 9, pp. 1070-1077.

Field Code Changed

9 LIST OF FIGURES

591 Figure 8. Numerical monotonic load-displacement curves.

592 Figure 9. a-d) In-plane principal stresses (S) and strains (E) in models dedicated to evaluate the influence
593 of opening size.

594 Figure 10. Numerical curves: Evaluation of eccentricity for a) (+x) Load and b) (-x) Load.

595 Figure 11. In-plane principal stresses (S) and strains (E) in model PW+L(d25e) at δ=+/-4.5 mm.

596 Figure 12. In-plane principal stresses (S) and strains (E) in model PW+L(d50e) at δ=+/- 4.5 mm.

597 Figure 13. a) Vertical load set-up and grinding disk used for cutting-out, b) temporary props used as
598 supports for the vertical load during the perforation process.

599 Figure 14. a) Arching actions on masonry due to vertical load and b) schematization of bed-joint crack
600 observed after the perforation process (approximate crack width=1 mm).

601 Figure 15. a) Final view of specimen PW+L(dc) after the steel lintel was introduced and b-c) cracks
602 observed after the perforation process.

603 Figure 16. Front view and side view of test setup.

604 Figure 17. Loading history.

605 Figure 18. Lateral Load-Displacement hysteresis for wall specimen PW+L(dc).

606 Figure 19. Experimental cracking patterns on specimen PW+L(dc), a) at δ=1.00 mm and b-c) at the end
607 of the test with two possible mechanisms of collapse, d) measured shear deformation with respect to the
608 imposed drift.

609 Figure 20. Experimental envelopes for walls PW+L(dc) ~~(tested in the present research)~~ and SW-R
610 ~~(~~tested ~~in~~ by Facconi et al., 2015~~)~~. ~~(Herein,~~ positive and negative loading directions are plotted in the
611 same quadrant). Note: bed-joint crack is coloured in red (pier 2).

Formatted: Font: Not Bold
Formatted: Font: Not Bold
Formatted: Font: Not Bold

612 Figure 21. Specimen PW+L: a) Experimental cracks, Front view (note: this specific photo was taken
613 after Phase 2, therefore only the cracks observed after Phase 1 are highlighted; b) numerical crack pattern
614 (at δ=6.6 mm) and corresponding crack width.

615

616 **10 LIST OF TABLES**

617 Table 1. Geometry and details of the walls in Figure 3.

618 Table 2: Summary of masonry material properties validated for the numerical models.

619 Table 3. Summary of experimental and numerical results for SW-R and PW+L(dc).

620

621

622

623

624

11 FIGURES AND TABLES IN ORDER OF APPEARANCE

a) b)

Figure 1. Example of new openings made at street-level of URM buildings in Brescia (Italy).

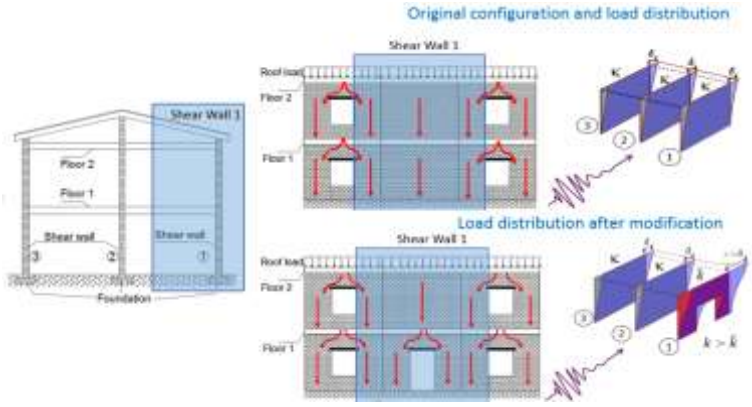

Figure 2. Lateral load redistribution when new openings are cut from structural URM walls.

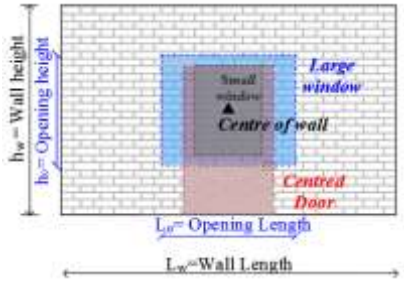

a)

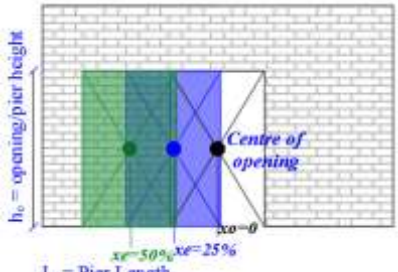

b)

Figure 3. Geometric configurations of the walls with openings herein studied.

Table 1: Geometry and details of the walls in Figure 3.

Wall	*Wall dimensions:*	*Opening dimensions*	*Opening Area (OA)*	*Opening Position (x_e)*	*Opening type*
	L_w x h_w [mm]	*L_o x h_o [mm]*	*(%)*		
SW-R	*3140x2000*	-	-	-	*Solid Wall -Reference*
PW+L(sw)		*630x840*	*8.5*	*Centred*	*Small Window*
PW+L(lw)		*1260x1050*	*21*		*Large Window*
PW+L(dc)		*840x1400*	*19*	*Centred*	*Door*
PW+L(d25e)				*Eccentric (x_e=25%)*	
PW+L(d50e)				*Eccentric (x_e=50%)*	

Formatted: Subscript

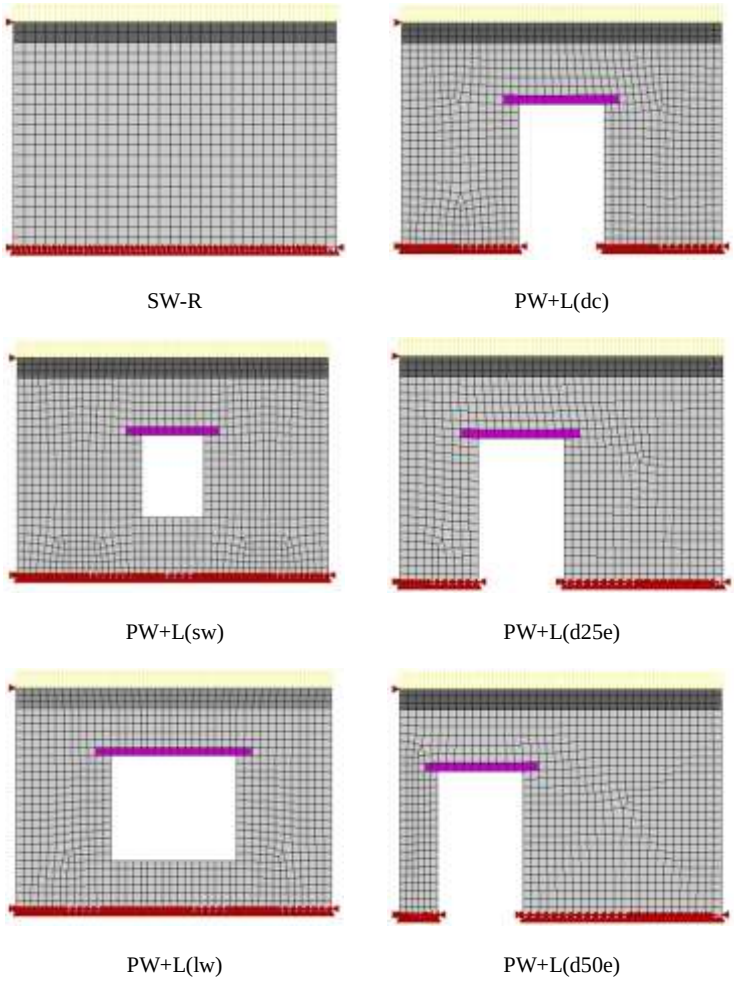

638 **Figure 4. Finite element mesh of the numerical models.**

639

Table 2: Summary of masonry material properties validated for the numerical models.

*Young Modulus**	*2700 MPa*
*Compressive strength**	*4.0 MPa*
Tensile strength^{++}	*0.14 MPa*
Compressive Fracture Energy^{+}	*5.0 N/mm*
Tensile Fracture Energy^{++}	*0.1 N/mm*
Shear Retention Factor	*0.01*

**Parameters based on the experimental tests carried out by Facconi (2013) and Facconi et al., 2015.*
$^{+}$50 times the tensile fracture energy, as suggested in Diana TNO Manual (2016).
$^{++}$ Due to the lack of experimental data, the tensile strength and the tensile fracture energy were obtained by performing numerical inverse analyses using the experimental results of Facconi et al., 2015.

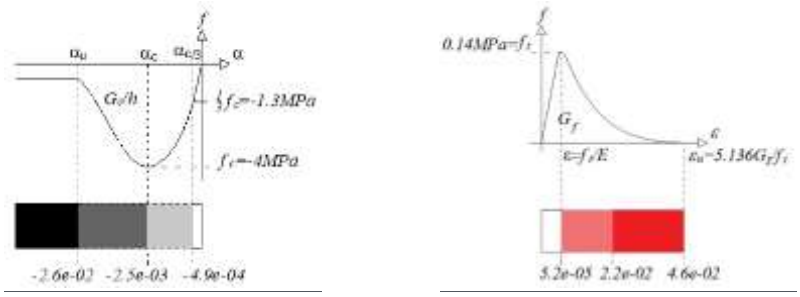

a) b)

Figure 5. a) Compression curve and b) tension curve used as constitutive relations.

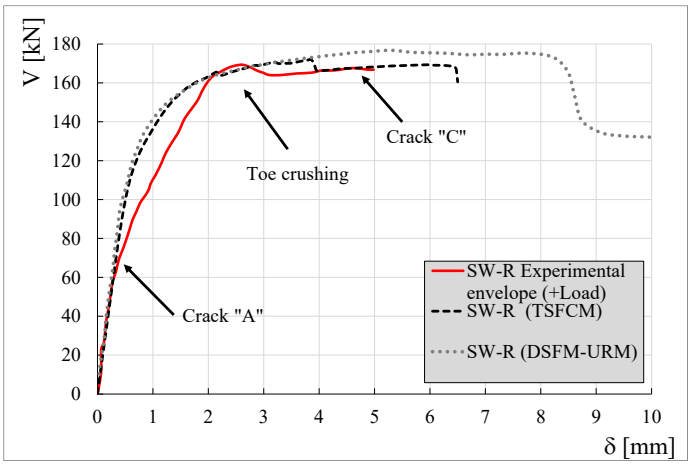

Figure 6. Comparison between experimental envelope and numerical curves.

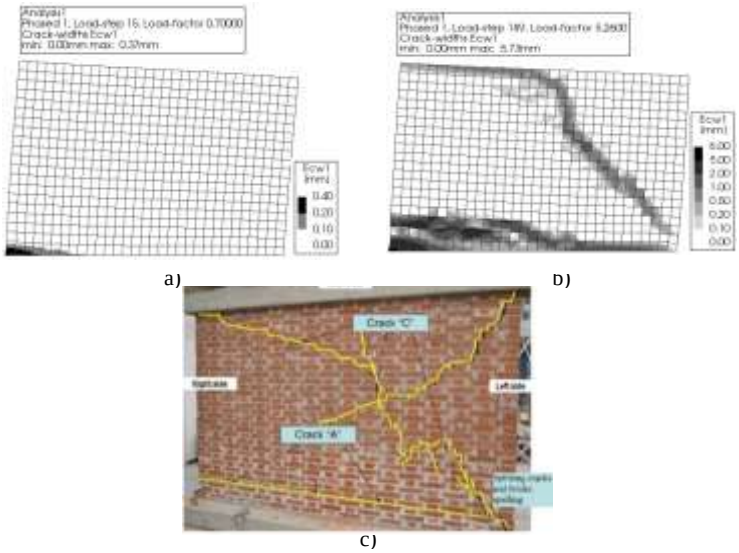

Figure 7. Comparison of numerical and experimental crack patterns, a) Numerical cracks at δ =0.7 mm; b) Numerical cracks at δ=5.26 mm; c) Experimental Cracks at 5 mm (Facconi et al., 2015). Note: numerical cracks are plotted as crack widths.

Formatted: Font: Italic

Formatted: Font: Italic

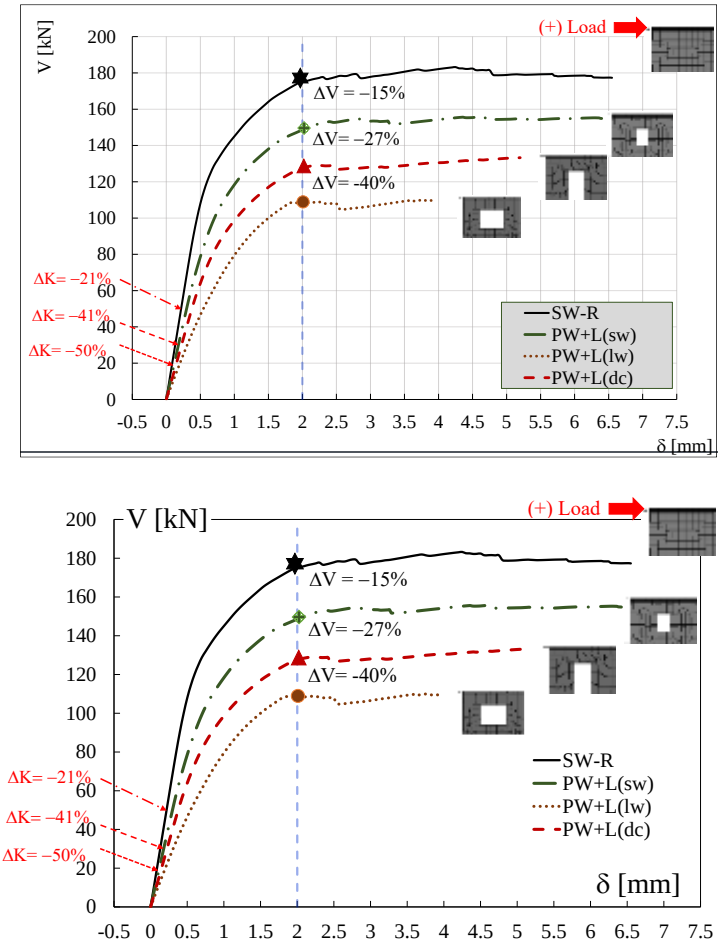

Figure 8. Numerical monotonic load-displacement curves.

659

660

661

662

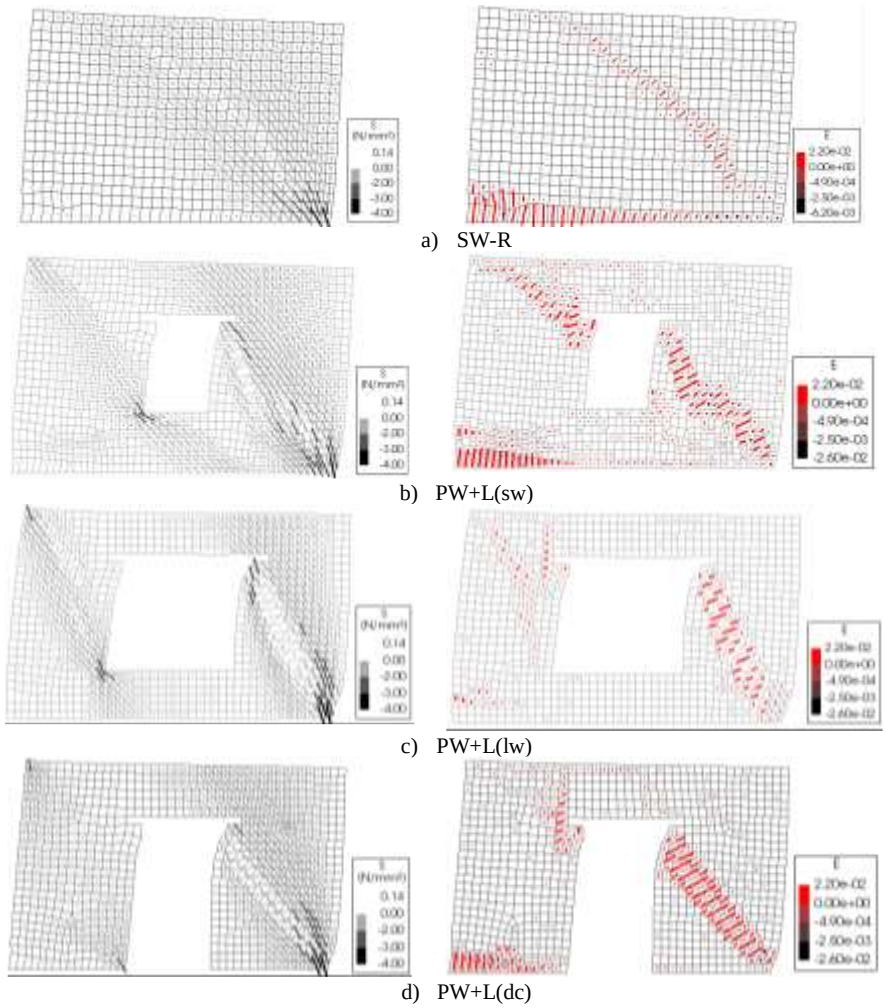

a) SW-R

b) PW+L(sw)

c) PW+L(lw)

d) PW+L(dc)

663 **Figure 9. a-d) In-plane principal stresses (S) and strains (E) in models dedicated to evaluate the**

664 **influence of opening size.**

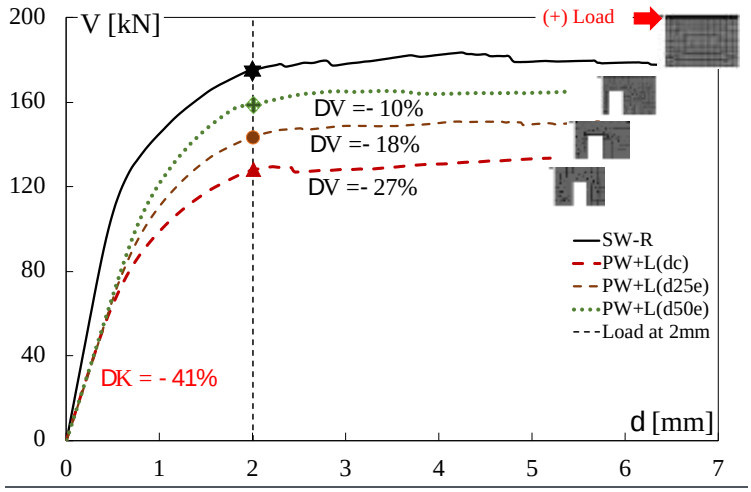
200
160
120
80
40
0
V [kN]
(+) Load
DV =- 10%
DV =- 18%
DV =- 27%
SW-R
PW+L(dc)
PW+L(d25e)
PW+L(d50e)
Load at 2mm
DK = - 41%
d [mm]
0
1
2
3
4
5
6
7

a)

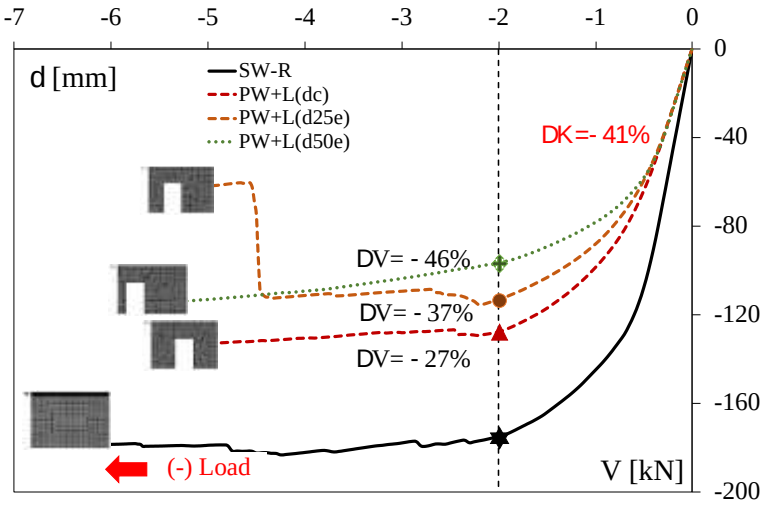
-7
-6
-5
-4
-3
-2
-1
0
d [mm]
SW-R
PW+L(dc)
PW+L(d25e)
PW+L(d50e)
DK=- 41%
DV= - 46%
DV= - 37%
DV= - 27%
(-) Load
V [kN]
0
-40
-80
-120
-160
-200

b)

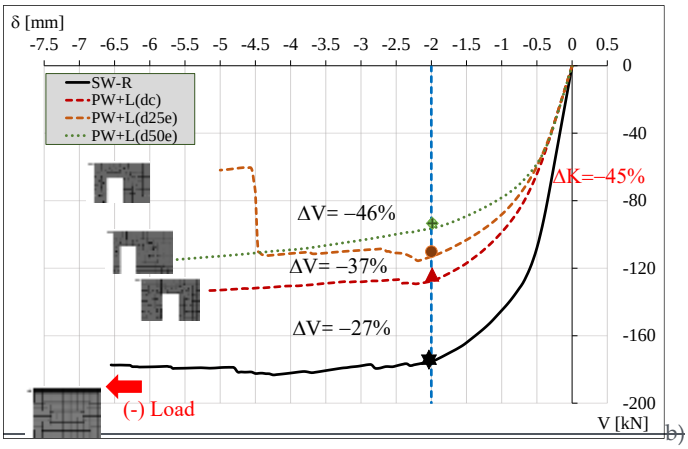

Figure 10. Numerical curves: Evaluation of eccentricity for a) Positive Load direction and b) Negative Load direction.

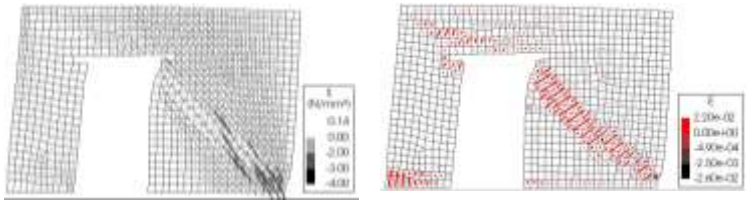

a) (+) Load direction

b) (+) Load direction

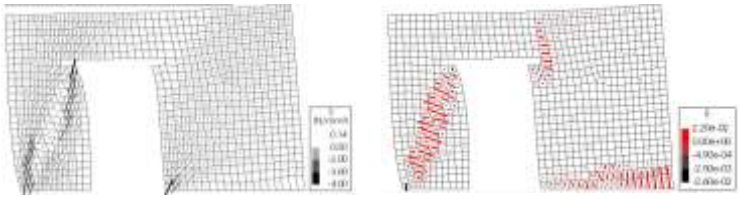

c) (-) Load direction

d) (-) Load direction

Figure 11. In-plane principal stresses (S) and strains (E) in model PW+L(d25e) at δ=+/-4.5 mm.

Formatted: Space After: 0 pt, Line spacing: Double

672

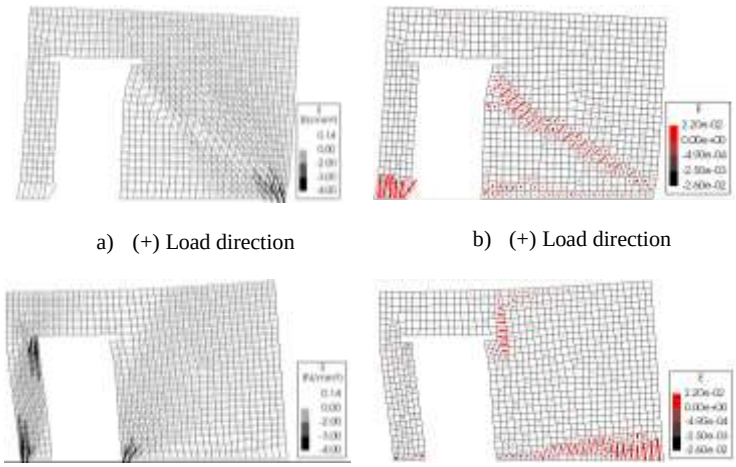

a) (+) Load direction b) (+) Load direction

c) (-) Load direction d) (-) Load direction

673 **Figure 12. In-plane principal stresses (S) and strains (E) in model PW+L(d50e) at δ=+/- 4.5 mm.**

Formatted: Justified

Formatted: Font: Italic

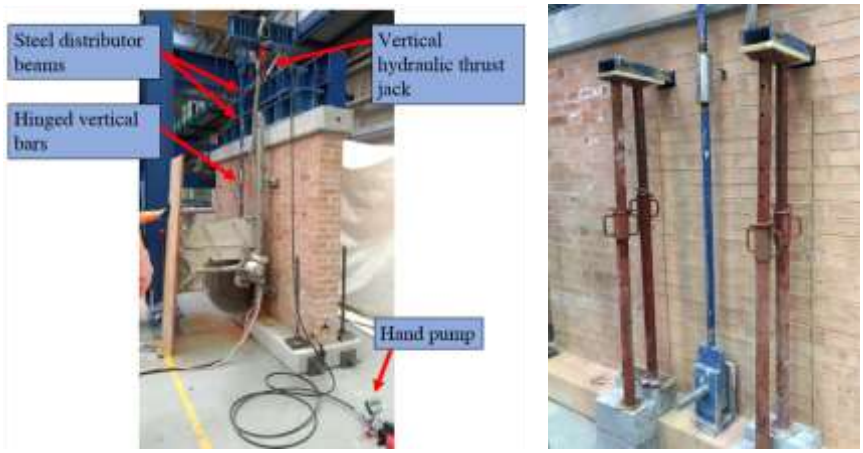

a) b)

674 **Figure 13. a) Vertical load set-up and grinding disk used for cutting-out, b) temporary props used**

675 **as supports for the vertical load during the perforation process.**

676

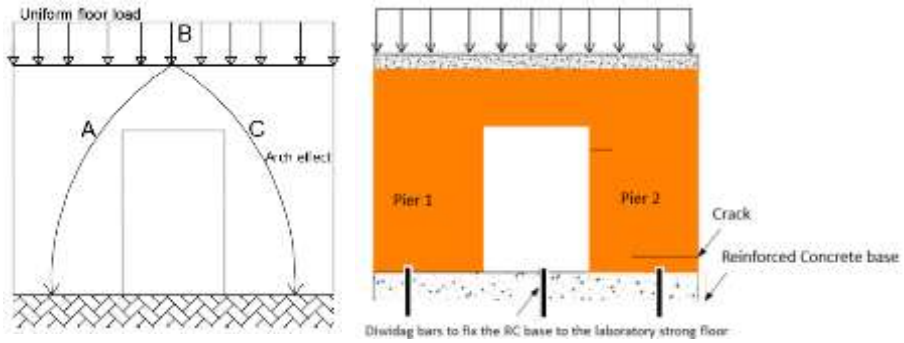

a) b)

677 **Figure 14. a) Arching actions on masonry due to vertical load and b) schematization of bed-joint**
678 **crack observed after the perforation process (approximate crack width = 1 mm).**

679

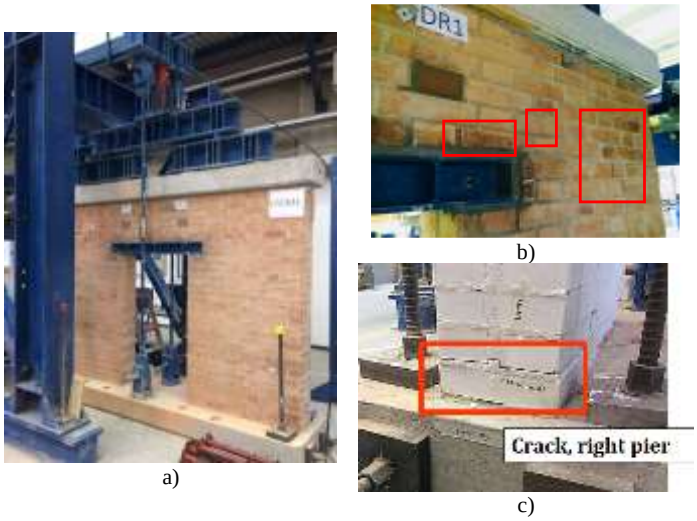

a) b) c)

680 **Figure 15. (a) Final view of specimen PW+L(dc) after the steel lintel was introduced and (b, c)**
681 **cracks observed after the perforation process.**

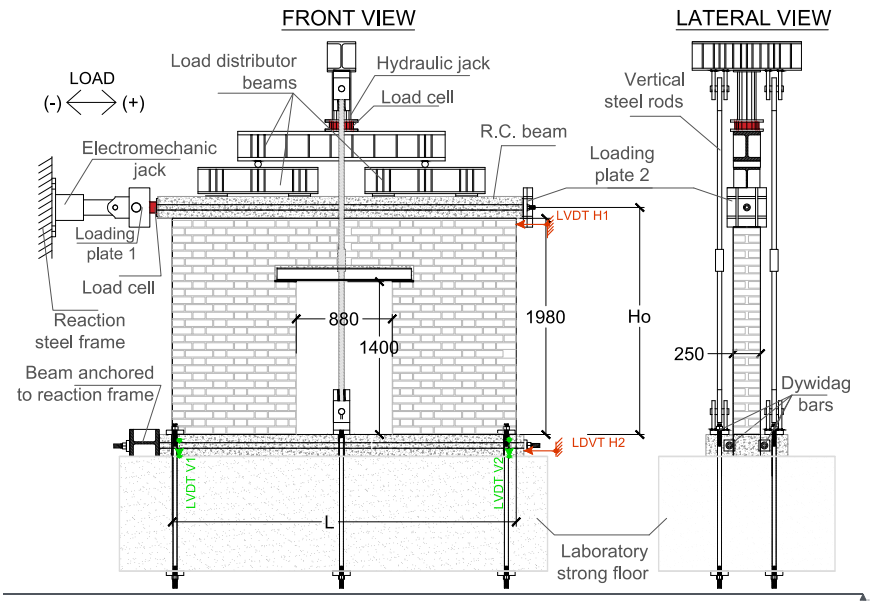

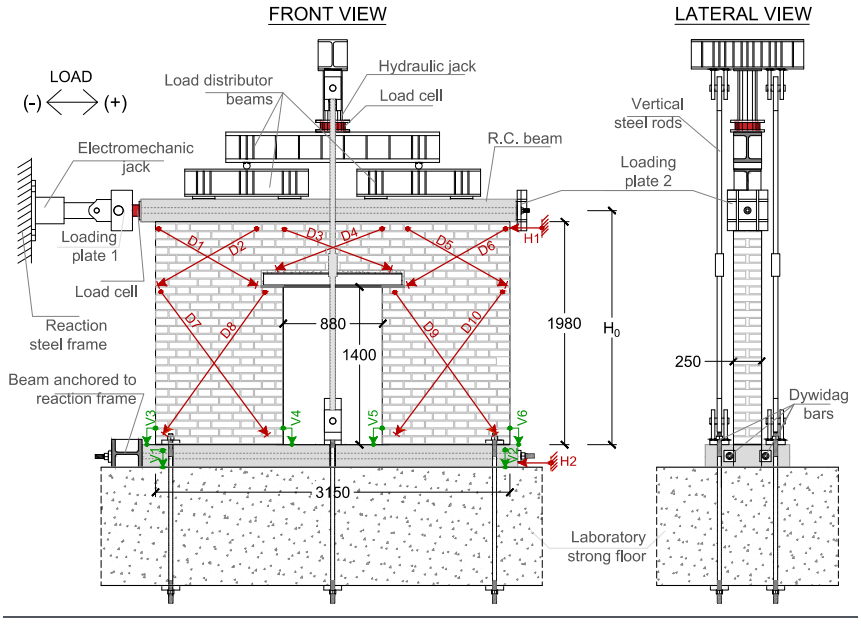

Figure 16. Front view and side view of test setup.

Formatted: English (United States)

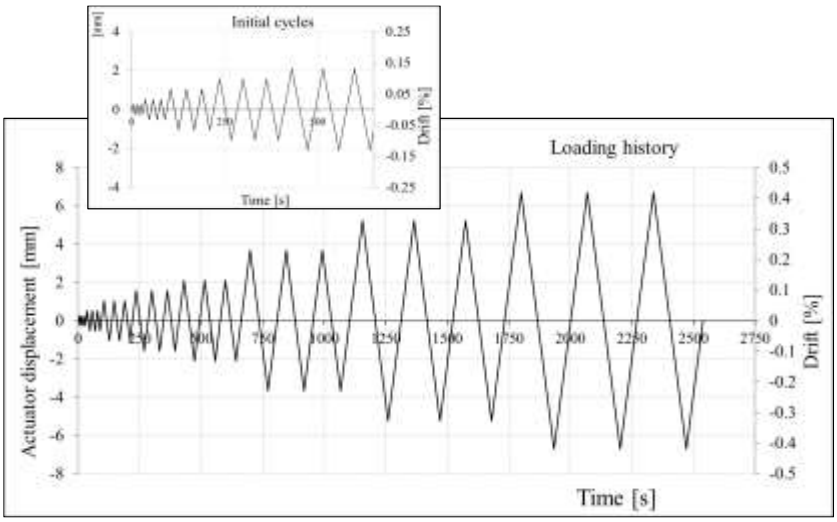

685

686 **Figure 17. Loading history.**

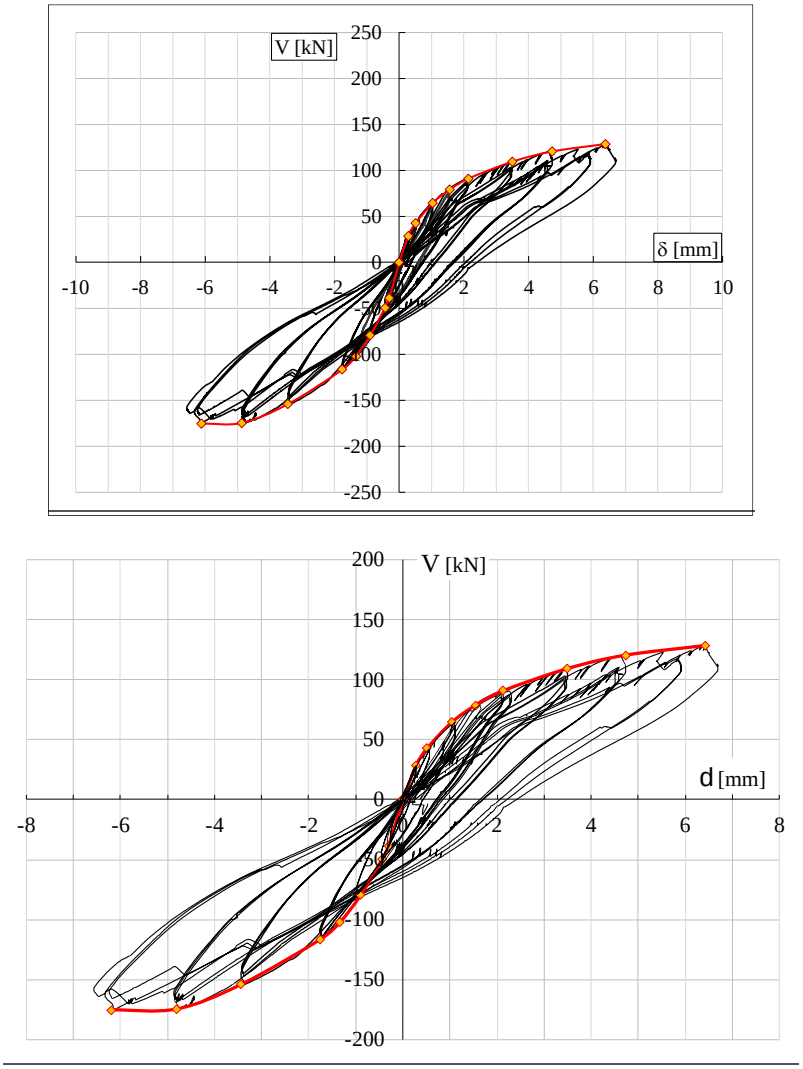

687

688

689 **Figure 18. Lateral Load-Displacement hysteresis for wall specimen PW+L(dc).**

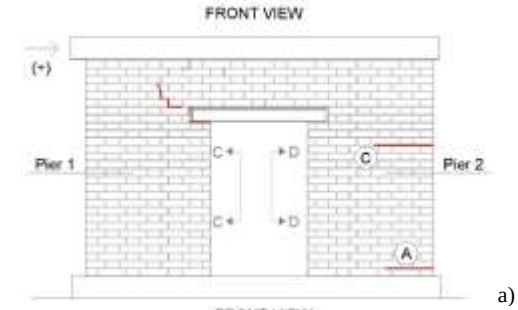

a)

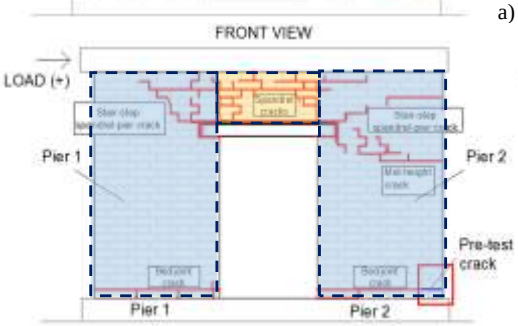

b)

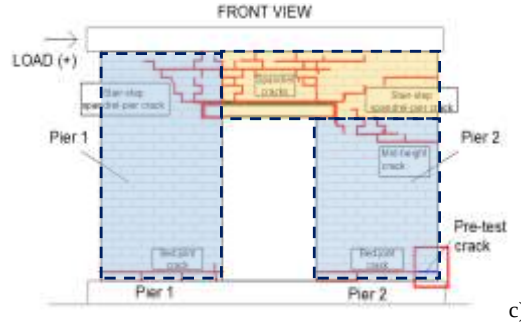

c)

Formatted: Indent: First line: 0 mm

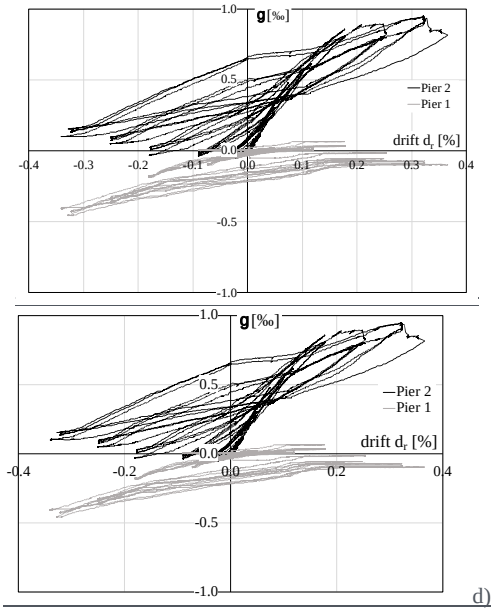

d)

Figure 19. Experimental cracking patterns on specimen PW+L(dc), a) at δ=1.00 mm and b-c) at the end of the test with two possible mechanisms of collapse, d) measured shear deformation with respect to the imposed drift. ~~In b-c) the two possible mechanisms of collapse are highlighted.~~

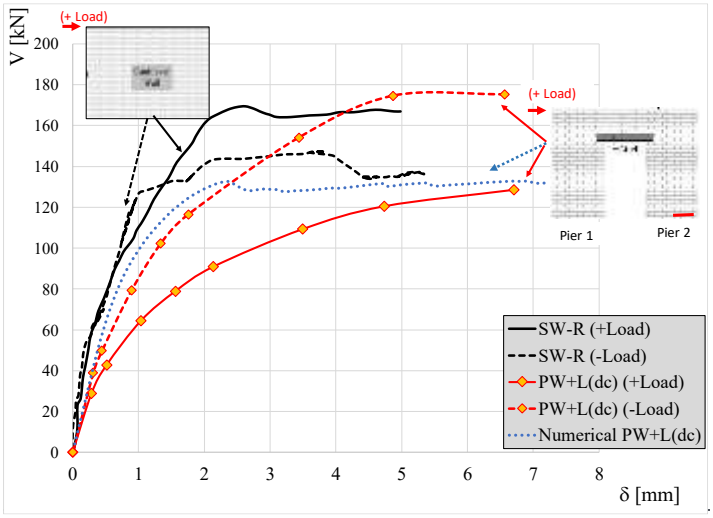

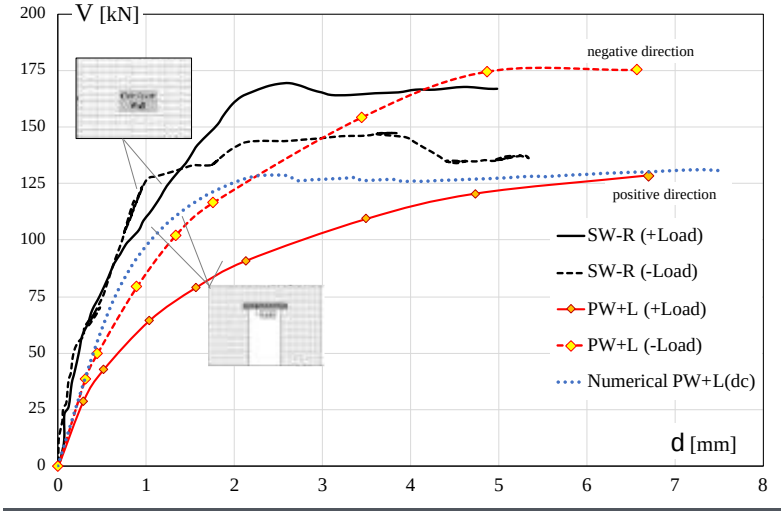

Figure 20. Experimental envelopes for walls PW+L(dc) and SW-R tested by Facconi et al., 2015 (positive and negative loading directions are plot in the same quadrant). Note: bed-joint crack is coloured in red (pier 2).

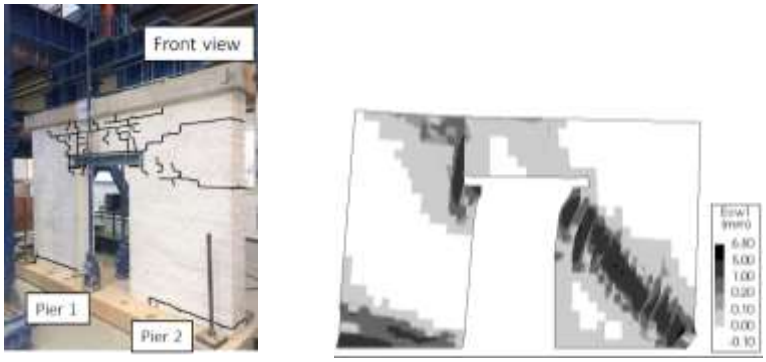

a) b)

Figure 21. Specimen PW+L: a) Experimental cracks, Front view (note: this specific photo was taken after Phase 2, therefore only the cracks observed after Phase 1 are highlighted; b) numerical crack pattern (at δ=6.6 mm) and corresponding crack width.

Table 3: Summary of experimental and numerical results for SW-R and PW+L(dc).

	Load direction	*K_e (δ=0.25mm) [kN/mm]*		*ΔK_e [%]*	*V_{peak} [kN]*		*$\Delta V_{,peak}$ [%]*
		*SW-R **	*PW+L(dc)*		*SW-R **	*PW+L(dc)*	
Experimental (cyclic)	*(+) Load*	*+208*	*+101*	*52*	*+167*	*+128.6*	*23*
	(-) Load	*-203*	*-125*	*38*	*-146*	*-175.2*	*20*
Numerical (monotonic)	-	*229*	*134*	*41*	*172*	*133*	*23*

*Data retrieved from Facconi et al. (2015).

Formatted: Italian (Italy)